Volume 6 | Number 32 | 28 August 2018 | Pages 15417–15890

Journal of Materials Chemistry A

Materials for energy and sustainability

rsc.li/materials-a

ISSN 2050-7488

PAPER

Hyunjung Lee *et al.*

Correlation between Seebeck coefficients and electronic structures of nitrogen- or boron-doped reduced graphene oxide *via* thermally activated carrier transport

Journal of
Materials Chemistry A

ROYAL SOCIETY OF CHEMISTRY

Published on 15 June 2018. Downloaded by Korea Institute of Science and Technology / KIST on 10/31/2019 6:27:51 AM.

PAPER

View Article Online
View Journal | View Issue

Cite this: *J. Mater. Chem. A*, 2018, **6**, 15577

Correlation between Seebeck coefficients and electronic structures of nitrogen- or boron-doped reduced graphene oxide *via* thermally activated carrier transport†

Hyunwoo Bark,[a] Wonmok Lee[b] and Hyunjung Lee*[a]

Received 18th April 2018
Accepted 13th June 2018

DOI: 10.1039/c8ta03545h

rsc.li/materials-a

In this study, we report the energy-level-dependent Seebeck coefficients of thermally reduced graphene oxide (TrGO) measured using a field-effect transistor with a microheater. B- or N-doped TrGO samples were prepared using graphene oxide (GO) solutions containing 10 or 50 mM boric acid or urea. In addition, heavily N-doped TrGO was prepared by annealing GO under an Ar/NH_3 atmosphere. During thermal annealing, boric acid and urea decomposed and B and N atoms were doped onto TrGO. The gate-dependent conductance of the samples was measured first. In general, all the samples exhibited ambipolar behavior. However, as a function of doping state, the gate-dependent conductance differed slightly in comparison with that of TrGO. B-TrGO exhibited more intensive hole transport, whereas N-TrGO exhibited more intensive electron transport. In addition, the conductance was investigated as a function of ambient temperature for evaluating bandgap opening by the doping effect. When the gate bias was changed from −80 to 80 V, the Seebeck coefficient of TrGO changed from 4 to −2 μV K^{-1}, which indicates that the carrier transport was changed from hole to electron transport depending on the energy state. However, impurity-doped TrGO (B- or N-TrGO) exhibited different behaviors. The Seebeck coefficient of B-TrGO changed from 20 to −4 μV K^{-1}, whereas that of N-TrGO changed from 4 to −10 μV K^{-1} in a similar range of gate bias. Notably, the Seebeck coefficient of heavily N-doped TrGO changed from −8 to −18 μV K^{-1} in a similar range of gate bias. On the basis of the Seebeck coefficients and relative bandgaps of TrGO, B-doped TrGO, and N-doped TrGO, the approximate relative electronic structure of TrGO was deduced.

Introduction

With the recent developments in the methods for preparing nanostructured materials or organic semiconductors and in the methods for fabricating devices with unique electronic properties,[1–5] the electronic structure of materials has become the most important consideration for ensuring their suitable application. Generally, the field-effect transistor has been a useful device for exploring the carrier transport properties of semiconductors.[6–8] With a survey of the conductance (G) of a semiconductor, its carrier transport properties are easily expressed. However, in the case of semimetal, zero-bandgap or ambipolar materials, the charge-carrier transport is difficult to clearly express on the sole basis of G because distinguishing the major charge carriers in the materials is difficult. Since Fritzsche's report on the theoretical aspects of the Seebeck coefficient (S),[9] the S has become an alternative parameter to G because the magnitude and sign of the S are determined by the electronic structure or the Fermi level of materials. Consequently, the S has been used to elucidate the precise electronic structures of materials. For example, Kim *et al.*[10,11] and Shi *et al.*[12] reported the thermoelectric properties of single-layer graphene exfoliated from graphite, which is a perfect structure of sp^2 hybridization.[10–12] Measurements of the thermoelectric properties as a function of energy level revealed that the charge-carrier type and the magnitude of the S of single-layer graphene changed at the charge-neutrality point. This continuous change of the S is consistent with metallic conduction, which occurs at the Fermi level, and Mott's model is applied to explain the metallic conduction:

$$S = -\frac{\pi^2 k_B{}^2 T}{3e}\frac{1}{G}\frac{dG}{dE}\bigg|_{E=E_F}$$

where k_B, e, and E are the Boltzmann constant, the elementary charge, and the energy level, respectively.

[a]School of Advanced Materials Engineering, Kookmin University, 77 Jeongneung-ro, Seongbuk-gu, Seoul, 02707, Republic of Korea. E-mail: hyunjung@kookmin.ac.kr
[b]Department of Chemistry, Sejong University, 209, Neungdong-ro, Gwangjin-gu, Seoul, 05006, Republic of Korea

† Electronic supplementary information (ESI) available. See DOI: 10.1039/c8ta03545h

This journal is © The Royal Society of Chemistry 2018

Published on 15 June 2018. Downloaded by Korea Institute of Science and Technology / KIST on 10/31/2019 6:27:51 AM.

Because the density of states of graphene is symmetric,[13] the magnitude or the sign of S is determined by the position of the Fermi level. For perfect single-layer graphene exfoliated from graphite, the lattice consists of carbon atoms with perfect sp^2 hybridization. Thus, the symmetric shape of the S as a function of the Fermi level is clearly revealed. Hu *et al.* prepared bilayer graphene separated by boron nitride and fabricated a double-gate device to determine its maximum power factor ($S^2\sigma$).[14] The carrier density of each graphene was controlled by top and bottom gates independently, and the maximum power factor was ~700 μW cm^{-1} K^{-2}. Park *et al.* prepared thermally reduced graphene oxide annealed at 1000 °C under an Ar/H_2 atmosphere and investigated its energy-dependent thermoelectric properties.[15] At 300 K, the S changed from −20 to 20 μV K^{-1} as a function of gate bias. Except for the aforementioned cases, the S of chemical vapor deposition (CVD)-grown graphene and reduced graphene oxide (rGO) have been measured at a fixed Fermi level. In the case of CVD-grown graphene, Lyeo *et al.*[16] and Li *et al.*[16,17] probed the S using atomic force microscopy (AFM) and scanning tunneling microscopy (STM). By using microscope probe tips to apply heat, they obtained images from which the S was derived and used the results to characterize defects on the graphene.

As previously explained, the S of metallic conductive materials is sensitive to the density of states and the position of the Fermi level. Because AFM- or STM-based S measurements involve atomic-scale observations, the local density of states in graphene is distorted by defects, boundaries, or wrinkles in the graphene, resulting in a change in the S. Yan *et al.* reported that the S of CVD-grown graphene increased with increasing oxygen plasma treatment.[18] When defects were generated in the graphene, the density of states was distorted and the S was enhanced.

The thermoelectric properties of rGO, which is used in various applications,[19,20] are much more complicated than those of graphene. Because rGO is prepared from graphene oxide (GO), the removal of oxygen functional groups is inevitable, and the work function of rGO varies as a function of the degree of oxidation.[21–23] Thus, rGO is an attractive alternative to bulk-scale inorganic-based thermoelectric materials because of its controllable energy state. In a previous report of the thermoelectric properties of rGO, control of the degree of oxidation using hydrazine enabled control of the electrical conductivity and the S; specifically, with increasing degree of reduction, the S decreased from 60 to 11 μV K^{-1}, whereas the electrical conductivity increased from 0.14 to 880 S m^{-1}.[24] Moreover, Kim *et al.* reported that the S of rGO prepared by thermal reduction varied with the reduction temperature.[25] Because the work function of rGO is changed by residual oxygen functional groups or defects, the rGO can exhibit n- or p-type character depending on the extent of reduction. Consequently, the S of CVD-grown GO or rGO depends on the synthesis or fabrication conditions. Conversely, if the S of CVD-grown GO or rGO can be measured precisely, their electronic structures or energy levels can be estimated.

Field-effect-modulated S measurements have also been used as an effective tool for evaluating the electronic structure of semiconductors. Pernstich *et al.*[26] and Sirringhaus *et al.*[26–28] have reported field-effect-modulated S measurements of organic semiconductors. They measured the S of organic semiconductors as a function of their electronic energy states using a field-effect-modulated Seebeck coefficient measurement system. In this device, the charge transport of materials is tuned *via* the gate bias in a field-effect transistor (FET) and the S is measured as a function of the gate bias. Nanostructured materials such as black phosphorus, graphene, carbon nanotubes, nanowires, and metal dichalcogenides have been similarly characterized by gate-bias-tuned S measurements.[10,29–34]

In the present study, field-effect-modulated S measurements of thermally reduced graphene oxide (TrGO) were conducted. To survey the electronic structure of TrGO precisely, devices with B- and N-doped TrGO were fabricated. From the Arrhenius plots of the electrical properties, the bandgap energies of TrGO, B-doped TrGO, and N-doped TrGO were obtained to observe the variations among their bandgaps. The gate bias (V_{Gate})-dependent S values were then examined. The contribution of charge carriers as a function of V_{Gate} was then determined, and the electronic structures of TrGO, B-doped TrGO, and N-doped TrGO were estimated.

Experimental section

Fabrication of impurity-containing GO solution

Graphite oxide was prepared using Hummers' method with graphite powder.[35] One gram of graphite powder (SP-1, Bay Carbon Inc., USA) and 0.5 g of $NaNO_3$ were dissolved in H_2SO_4 (25 mL) with stirring for 1 h. The reaction was conducted in an ice bath. Three grams of $KMnO_4$ was added to the acid solution with stirring for 1 h. The temperature was then increased gradually to 35 °C. Forty-six milliliters of H_2O was added to the mixture, followed by the addition of a hydrogen peroxide solution (H_2O/H_2O_2 = 140 : 2.5, mL : mL). The obtained product was washed sequentially with 10% HCl solution and H_2O and was then freeze-dried. Twenty milligrams of dried graphite oxide powder were dispersed in 20 mL of H_2O using a bath-type sonicator, followed by centrifugation at 3000 rpm for 5 min. The supernatant (GO solution) was collected in a vial. B- or N-doped rGO was prepared using boric acid (ACS reagent, Sigma-Aldrich) or urea (BioReagent, Sigma-Aldrich), respectively, as dopants. GO solutions containing 10 or 50 mM of boric acid or urea were prepared.

Fabrication of the FET-based Seebeck coefficient measurement device

To investigate the electrical properties and S of the TrGO samples, we fabricated an FET-based S measurement device. First, the prepared GO solution, boric-acid-containing GO solution, or urea-containing GO solution was spin-coated twice onto a cleaned substrate (Si/SiO_2, 300 nm, heavily doped) at 500 rpm (30 s) and 2000 rpm (10 s). The GO on the substrate was thermally reduced at 1173 K for 2 h under an Ar atmosphere; to obtain TrGO heavily doped with N, thermal reduction was conducted under Ar/NH_3. After reduction, the active layer (rGO)

Published on 15 June 2018. Downloaded by Korea Institute of Science and Technology / KIST on 10/31/2019 6:27:51 AM.

was obtained by photolithography. A positive photoresist was spin-coated onto the substrate, and the substrate was baked at 373 K for 90 s. Ultraviolet (UV) exposure was conducted with the active-layer region of the substrate covered with a photomask. After the exposure, the substrate was dipped in developer solution for 30 s, and the photoresist was removed except for that on the active layer. The residual rGO was removed using O_2 plasma (100 W, 5 min). To fabricate an electrode and a micro-heater, photolithography was conducted again. The electrode (Ti/Au, 10 nm/10 nm) of the device was deposited using an e-beam evaporator for the Ti and using thermal evaporation for Au. The channel length (L) and width (W) of the materials were 50 and 1000 μm, respectively. A schematic of the fabrication process is illustrated in Fig. S1.†

Characterization

The carrier transport properties (G and S) and the temperature gradient (ΔT) were examined under high vacuum. To obtain the ΔT in the FET-modulated S measurement device, the temperature coefficient of resistance (TCR) in the hot side and cold-side electrodes was measured between 203 and 330 K. The ambient temperature at the surface of the substrate was recorded using a T-type thermocouple and data logger (Keithley 2700, data acquisition system). The resistances of the hot side and cold-side electrodes were measured as a function of the ambient temperature using a dual-channel source meter (Keithley 2613B), and the resistance was plotted as a function of the ambient temperature. The slope obtained from a linear fit of the data was the TCR. After obtaining the TCR, we examined the dependence of the electrode resistance on the applied current in the region of the heater with a temperature gradient (Fig. S10–S14†). A single-channel source meter (Keithley 2400) was used to supply current to the heater. Each current step was applied for 30 s, and the resistances were obtained at 303 K. The resistances were then converted into temperatures using the following equations:

$$T_{\text{hot side}} = 303\ \text{K} + \left(\frac{R_{\text{power,hot side}} - R_{0,\text{hot side}}}{\text{TCR}_{\text{hot side}}}\right)$$

$$T_{\text{cold side}} = 303\ \text{K} + \left(\frac{R_{\text{power,cold side}} - R_{0,\text{cold side}}}{\text{TCR}_{\text{cold side}}}\right)$$

$$\Delta T = T_{\text{hot side}} - T_{\text{cold side}}$$

where $T_{\text{hot side (cold side)}}$, $R_{\text{power,hot side (cold side)}}$, $R_{0,\text{hot side (cold side)}}$, and $\text{TCR}_{\text{hot side (cold side)}}$ are the temperatures of the hot side (cold side), the resistance of the hot side (cold side) with power applied to the heater, the resistance of the hot side (cold side) without power applied to the heater, and the TCR for the hot side (cold side), respectively. The heater power (P) was calculated using $P = V \times I$.

The generated voltage as a function of the step current was detected using a nanovoltmeter (Keithley 2182A). The S was obtained as the slope of ΔT plotted against the generated voltage (ΔV). The S as a function of the gate bias was obtained by applying a bias of 5 V. The electrical properties were measured using a dual-channel source meter (Keithley 2613B).

Results and discussion

As illustrated in Scheme 1 (and Fig. S1†), the solution process was used to prepare samples for use in the gate-dependent S measurement device. To compare the carrier transport of TrGO with different energy states, TrGO samples doped with B or N were also prepared.

Before investigating the carrier transport properties, we examined the reduction conditions and doping degree of the samples by X-ray photoelectron spectroscopy (XPS). Fig. S2† shows the XPS spectra of GO, TrGO, 10 mM B-TrGO, 50 mM B-TrGO, 10 mM N-TrGO, 50 mM N-TrGO, and NH_3 N-TrGO from 0 to 850 eV. Generally, peaks attributed to C and O appeared in the spectra of all the samples. After the GO was annealed, the intensity of the O peak decreased, whereas that of the C peak increased. A comparison of the atomic composition before and after reduction, as presented in Table 1, reveals that the O atomic ratio decreased from approximately 24 to 4.5 at% after reduction. Because the reduction process was conducted under an Ar atmosphere, sp^2 hybridization of GO was recovered and oxygen functional groups were removed.

In the case of doped TrGO (B-TrGO or N-TrGO), an additional peak associated with B or N, respectively, was observed in the

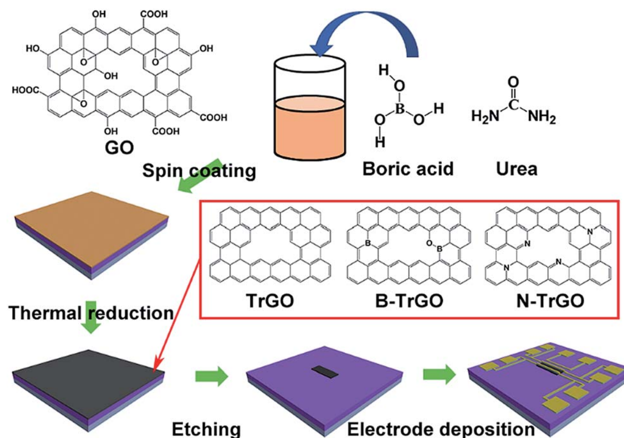

Scheme 1 Schematic of the preparation of various-energy-state TrGO for gate-dependent Seebeck coefficient measurements.

Table 1 Atomic ratio of GO, TrGO, 10 mM B-TrGO, 50 mM B-TrGO, 10 mM N-TrGO, 50 mM N TrGO, and NH_3 N-TrGO

Sample	C (at%)	O (at%)	N (at%)	B (at%)
GO	75.78 ± 0.53	24.22 ± 0.63	—	—
TrGO	95.52 ± 0.25	4.48 ± 0.12	—	—
10 mM B-TrGO	83.88 ± 1.67	12.68 ± 1.51	—	3.44 ± 0.17
50 mM B-TrGO	79.4 ± 0.1	16.51 ± 0.35	—	4.08 ± 0.25
10 mM N-TrGO	90.88 ± 0.41	4.7 ± 0.46	4.42 ± 0.16	—
50 mM N-TrGO	89.65 ± 0.99	5.7 ± 0.69	4.65 ± 0.49	—
NH_3 N-TrGO	90.73 ± 0.45	3.82 ± 0.39	5.45 ± 0.23	—

Published on 15 June 2018. Downloaded by Korea Institute of Science and Technology / KIST on 10/31/2019 6:27:51 AM.

spectrum. In the case of B-doped TrGO, the atomic percentages of B in the 10 mM B-TrGO and 50 mM B-TrGO were approximately 3.44 and 4.08 at%, respectively. The atomic percentages of O in 10 mM B-TrGO and 50 mM B-TrGO (12.68 and 16.51 at%) were higher than that the atomic percentage of O in TrGO (4.48 at%). Even though the reduction temperatures of the samples were similar, the percentage of O increased because of the impurity (boric acid). The spectra indicated that N atoms were present in the N-doped samples. All the N-TrGO samples had N contents greater than 4 at%. The 10 mM N-TrGO and 50 mM N-TrGO had N contents of 4.42 ± 0.16 and 4.65 ± 0.49 at%; these values are unrelated to the impurity concentration. However, in NH_3 N-TrGO (heavily doped N-TrGO), the at% of N increased to 5.45 at%. To elucidate the reduction state or chemical bonding in the rGO, we collected its C 1s XPS spectrum (Fig. 1(a)), which reveals the extensive presence of oxygen functional groups. Specifically, the C 1s spectrum of GO includes four main components: C=C (284.7 eV), C–OH (285.9 eV), C–O–C (287.2 eV), and C=O/COOH (288.7 eV). After thermal reduction, the C=C peak intensity in the spectrum of TrGO (Fig. 1(b)) was recovered and the intensity of the peaks associated with oxygen functional groups decreased. Additional peaks (C–B: 283.8 eV, C–N: 285.8 eV) were detected in the spectra of B-TrGO and N-TrGO, respectively (Fig. S3†). These additional peaks imply that the impurity atoms (B or N) were doped onto the TrGO. To survey the B and N in the graphene lattice in greater detail, we acquired B 1s and N 1s spectra of 10 and 50 mM B-TrGO (Fig. 1(c) and (d)), 10 and 50 mM N-TrGO (Fig. 1(e) and (f)), and NH_3 N-TrGO (Fig. 1(g)). In the B 1s spectrum, two major peaks associated with BC_2O (191 eV) and BC_3 (193 eV) are observed, consistent with previous reports.[36,37] B-doped rGO and CVD-grown graphene are known to exhibit p-type character.[38–40] The electrical properties of 10 mM B-TrGO and 50 mM B-TrGO are discussed later in this work. As previously noted, the existence of BC_2O in 10 mM B-TrGO and 50 mM B-TrGO resulted in higher oxygen percentages in 10 mM B-TrGO and 50 mM B-TrGO compared with that in TrGO.

The N 1s spectra of 10 mM N-TrGO, 50 mM N-TrGO, and NH_3 N-TrGO (Fig. 1(e–g), respectively) all show two major peaks, which are attributed to pyridinic N (~398.4 eV) and graphitic N (~401.6 eV). The spectra show that most of the N was graphitic N. Specifically, the area percentage of graphitic N of the 10 mM N-TrGO, 50 mM N-TrGO, and the NH_3 N-TrGO was 58.07, 57.63, and 66.69%, respectively. Even though the 10 mM N-TrGO, 50 mM N-TrGO, and NH_3 N-TrGO were reduced at similar temperatures, the graphitic N peak area in the spectrum of the NH_3 N-TrGO was the most intense. Therefore, the NH_3 N-TrGO is considered to be heavily N-doped. The graphitic N in rGO is important for obtaining n-type rGO.[41]

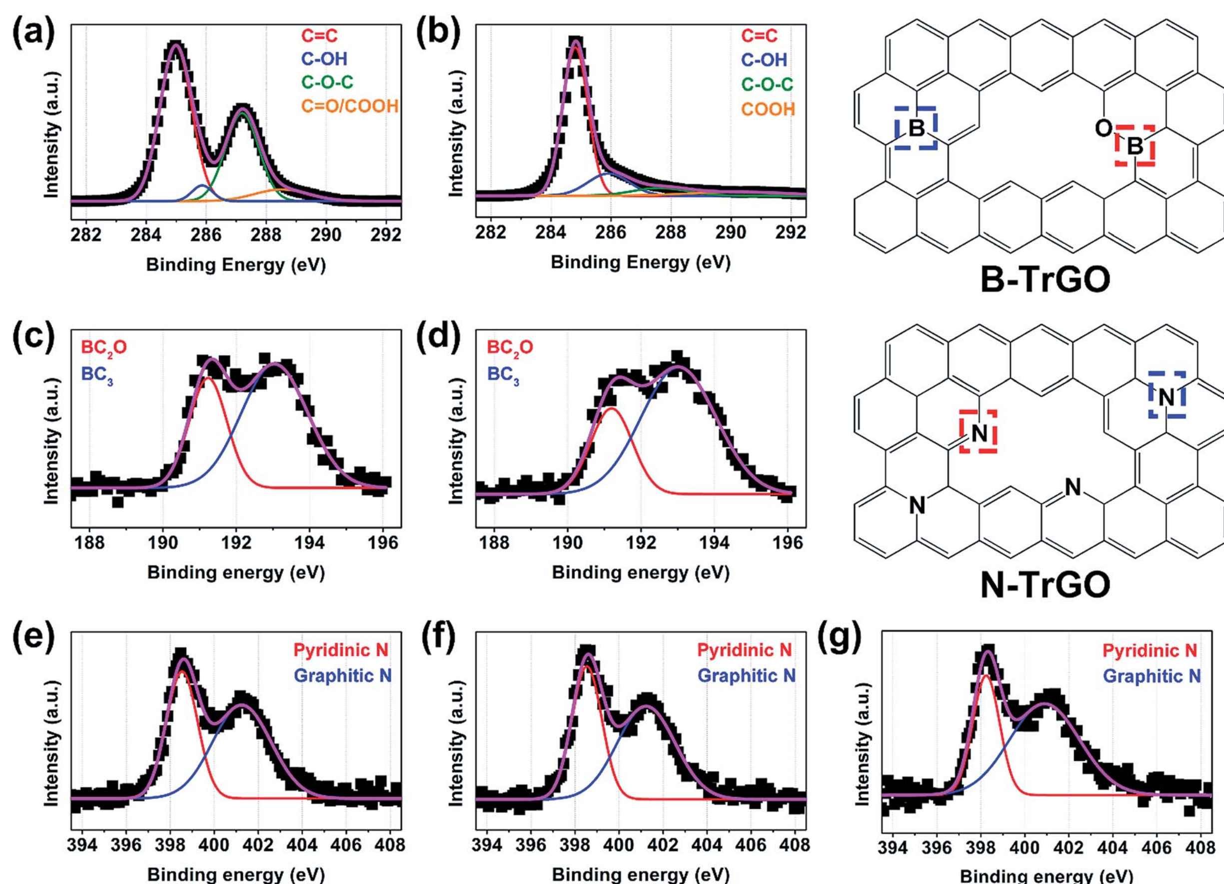

Fig. 1 XPS spectra of the TrGO samples: (a) C 1s of GO, (b) C 1s of TrGO, (c) B 1s of 10 mM B-TrGO, (d) B 1s of 50 mM B-TrGO, (e) N 1s of 10 mM N-TrGO, (f) N 1s of 50 mM N-TrGO, and (g) N 1s of NH_3 N-TrGO.

 This journal is © The Royal Society of Chemistry 2018

Published on 15 June 2018. Downloaded by Korea Institute of Science and Technology / KIST on 10/31/2019 6:27:51 AM.

Fig. S4† illustrates the morphology of the fabricated devices with TrGO. Fig. S4(a)† shows an optical microscopy image of TrGO. The blue-shaded part is the active layer, which is TrGO, and the rose/gold part is the electrode for sensing thermally activated potential or generating heat. The AFM images in Fig. S4(b)† show a survey of the thickness of the device. The thickness of the device was 5.55 nm. The other devices based on 10 mM B-TrGO, 50 mM B-TrGO, 10 mM N-TrGO, 50 mM N-TrGO, and NH_3 N-TrGO have thicknesses less than 6 nm, as illustrated in Fig. S5–S9,† respectively. As previously noted, the monolayer of GO was ~1 nm thick. The AFM analysis reveals that approximately 5 to 6 layers were present in TrGO. Part of the active layer was covered with rGO (Fig. S4(c)†).

To compare the transport properties between electrons and holes, we divided the G as a function of V_{Gate} by the minimum conductance (G_{min}). Fig. 2 shows G/G_{min} at room temperature plotted as a function of V_{Gate} for TrGO (Fig. 2(a)), 10 mM B-TrGO (Fig. 2(b)), 50 mM B-TrGO (Fig. 2(c)), 10 mM N-TrGO (Fig. 2(d)), 50 mM N-TrGO (Fig. 2(e)), and NH_3 N-TrGO (Fig. 2(f)), where V_{Gate} is the gate voltage. The G was converted using the equation $G = (I_{Drain}/V_{Drain})(L/W)$, where I_{Drain} and V_{Drain} are the drain current and the drain voltage, respectively. The transfer curves show that all the samples exhibited ambipolar behavior, which indicates that both electron and hole transport were induced by the applied V_{Gate}. However, depending on the doping state, electron transport and hole transport differed slightly. In the case of TrGO (Fig. 2(a)), even though TrGO exhibited ambipolar transport, holes exhibited better transport than electrons in this material. At $V_{Gate} = -80$ V (hole-transport-inducing), the G increased by approximately 10% compared with the G_{min}, whereas at $V_{Gate} = 80$ V (electron-transport-inducing), the G increased by approximately 4%. The higher hole transport of TrGO was speculatively attributed to the residual oxygen functional groups or to several defects on TrGO. After B doping on TrGO (Fig. 2(b) and (c)), the hole transport of both 10 and 50 mM B-TrGO was greater than that of TrGO, but the hole transport of B-doped TrGO was independent as a function of boric acid concentration. Even though the boron content in 50 mM B-TrGO was higher than that of 10 mM B-TrGO, the hole transport of 50 mM B-TrGO was lower than that of 50 mM B-TrGO, which is suspected by the increase of oxygen content. At lower oxygen contents, TrGO showed intensive hole transport.[42] With the higher concentration of boric acid, boron doping occurred with an increase of oxygen content. Lower hole transport in 50 mM B-TrGO is suspected by the increase of oxygen content, which causes suppression of hole transport. Conversely, after N doping on TrGO (Fig. 2(d)–(f)), the electron transport increased. Because TrGO exhibited more intensive hole transport initially, the G levels at the hole-transport-inducing V_{Gate} (−80 V) and electron-transport-inducing V_{Gate} (80 V) with 10 mM N-TrGO and 50 mM N-TrGO were similar; however, the electron transport of 10 mM N-TrGO and 50 mM N-TrGO was enhanced by the doping effect. Notably, in the case of NH_3 N-TrGO (Fig. 2(f)), the electron transport was substantially enhanced.

To elucidate the electronic structure of TrGO, 10 mM B-TrGO, 50 mM B-TrGO, 10 mM N-TrGO, 50 mM N-TrGO, and NH_3 N-TrGO, we carried out temperature-dependent measurements of their electrical properties and constructed Arrhenius plots (Fig. 3). For the Arrhenius plots, the transfer curves of all the samples were measured from 150 to 375 K. The G_{min} at each temperature was used to exclude the effect of impurities.[43] The $\ln(G_{min})$ was examined as a function of $1/T$. The following equation was used to calculate the bandgap energy of all the samples:[44]

$$G = G_0 \exp(-E_g/2kT)$$

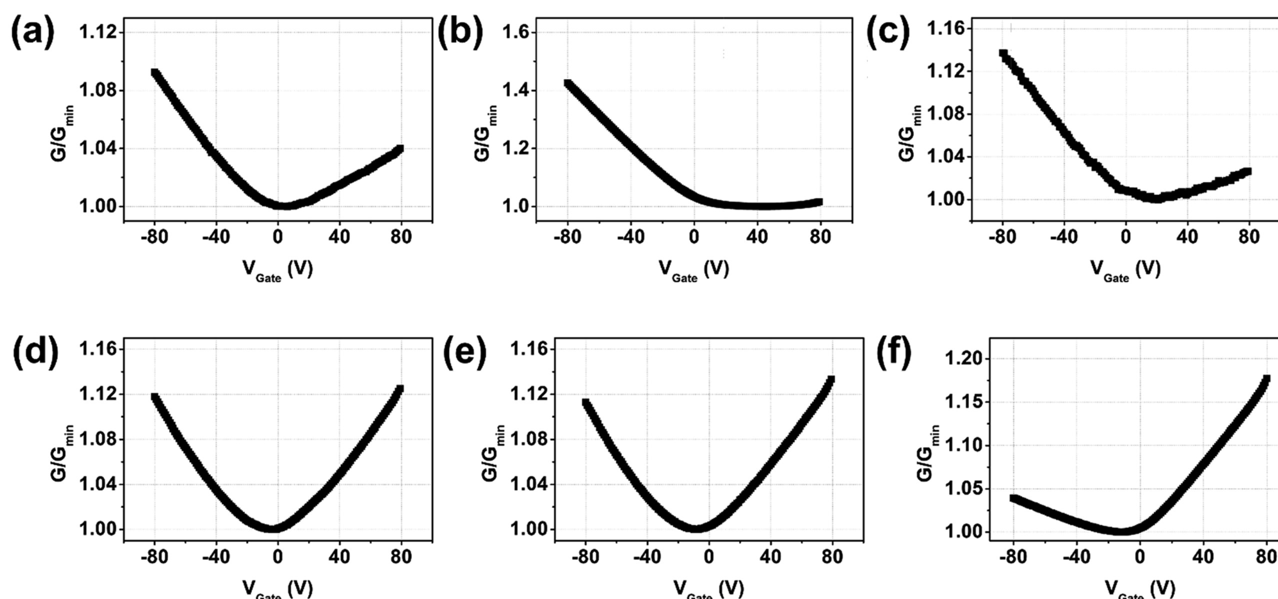

Fig. 2 Transfer curves of (a) TrGO, (b) 10 mM B-TrGO, (c) 50 mM B-TrGO, (d) 10 mM N-TrGO, (e) 50 mM N-TrGO, and (f) NH_3 N-TrGO with $V_{Drain} = -1$ V and p-sweep of V_{Gate}.

Published on 15 June 2018. Downloaded by Korea Institute of Science and Technology / KIST on 10/31/2019 6:27:51 AM.

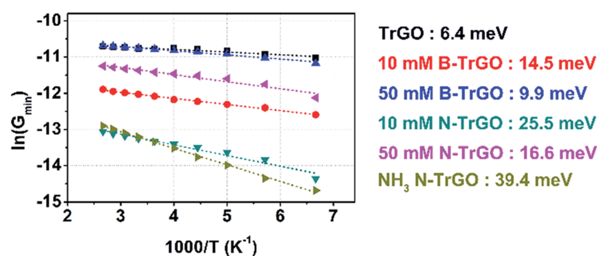

Fig. 3 Arrhenius plots of TrGO, 10 mM B-TrGO, 50 mM B-TrGO, 10 mM N-TrGO, 50 mM N-TrGO, and NH_3 N-TrGO.

where E_g and T are the bandgap energy and the absolute temperature, respectively.

Generally, the activation energies of 10 mM B-TrGO (14.5 meV), 50 mM B-TrGO (9.9 meV), 10 mM N-TrGO (25.5 meV), 50 mM N-TrGO (16.6 meV), and NH_3 N-TrGO (39.4 meV) were higher than the activation energy of TrGO (6.4 meV). Even though the electronic structure of multi-layered graphene is similar to that of graphite,[45] an increase of E_g was detected after doping. The electronic structure of doped TrGO was distorted, resulting in an asymmetric electronic structure.[46]

To understand the asymmetric electronic structures of N- or B-doped TrGO, we examined carrier transport properties such as G and S values as a function of temperature gradient (ΔT) under high vacuum. The ΔT in the FET-modulated S measurement device was first obtained. The TCR in the hot side and cold side electrodes was measured at between 203 and 330 K. The TCR was obtained as the slope of the linear fitting of the plot of resistance (R) *vs.* T, as illustrated in Fig. 4(a). In the case of TrGO, the TCRs of hot side and cold side were 1.17 ± 0.02 and $1.17 \pm 0.01\ \Omega\ K^{-1}$, respectively. The other TCRs of the devices are shown in Fig. S10(a), S11(a), S12(a), S13(a), and S14(a).†

After obtaining the TCR, we examined the resistances of the electrodes as a function of current applied to the heater portion to create a temperature gradient (Fig. 4(b)). The method used to evaluate ΔT has been previously applied to characterize the thermoelectric properties of nanostructured materials or organic semiconductors.[11,27,47–49] A single-channel source meter was used to supply current to the heater. The current for Joule heating at the heater ranged from 15 to 35 mA with a 5 mA current step at 303 K. Each current step was applied for 30 s, and the resistances were measured. After the resistances of the hot side and cold side were measured without current supplied to the heater (R_0), the resistances at the hot side and cold side were surveyed as a function of the current step. The resistance gradient and the temperature of the hot side and cold side are illustrated in Fig. 4(b), (top and middle). The temperature gradient of TrGO reached approximately 0.85 K, as shown in Fig. 4(b), (bottom). The temperature-gradient calibrations of the other devices are depicted in Fig. S10(b), S11(b), S12(b), S13(b), and S14(b).†

After evaluation of ΔT, the potential gradient (ΔV) was measured as a function of ΔT, from which the S was obtained as the slope of the linear fit of the data. The generated voltage as a function of the current step was measured. The S was obtained as the slope of the fitted line of ΔT *versus* ΔV. The S as a function of the gate bias was obtained by applying a bias of 10 V. To evaluate the potential gradient precisely, we subtracted the potential in the absence of heater power ($\Delta T = 0$ K) from the potential with applied heater power ($\Delta T > 0$ K). In addition, the S was measured as the V_{Gate} was changed from −80 to 80 V in 10 V steps. The linear fit of TrGO is expressed in Fig. 5; the linear fits for the other devices are shown in Fig. S15–S19.†

When V_{Gate} was changed from −80 to 80 V, the slope (S) of TrGO changed from approximately 4 to $-2\ \mu V\ K^{-1}$ at 303 K, which is consistent with ambipolar transport. Fig. 6(a) shows the gate-dependent S for all the samples at 303 K. The gate-dependent S of all of the samples changed gradually, and the absolute value of the S was less than $20\ \mu V\ K^{-1}$ in the gate-bias range from 80 to −80 V, which suggests an almost constant density of states or multiple sub-bands of multi-layered rGO.[50] In accordance with ambipolar transport in the transfer curve of TrGO, S as a function of V_{Gate} for TrGO shows a similar

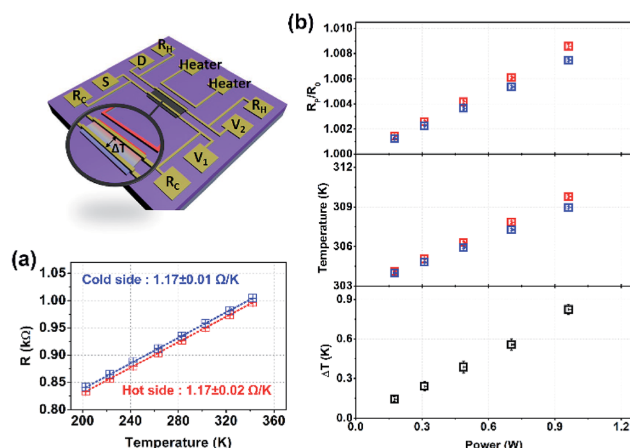

Fig. 4 Schematic of the gate-dependent Seebeck coefficient measurement device and (a) the TCR of TrGO, (b) the resistance gradient of the hot side (red open squares) and the cold side (blue open squares) (top), the temperature of the hot side and the cold side (middle), and the temperature gradient of the TrGO as a function of heater power.

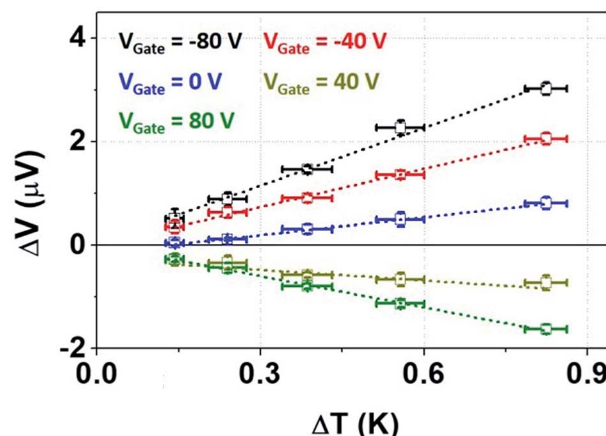

Fig. 5 Example of linear fitting for determining the Seebeck coefficient of TrGO with $V_{Gate} = -80, -40, 0, 40$, and 80 V.

This journal is © The Royal Society of Chemistry 2018

Published on 15 June 2018. Downloaded by Korea Institute of Science and Technology / KIST on 10/31/2019 6:27:51 AM.

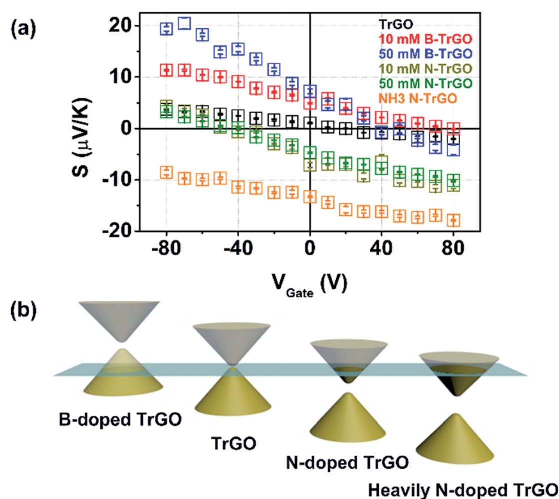

Fig. 6 (a) Gate-dependent Seebeck coefficient of TrGO, 10 mM B-TrGO, 50 mM B-TrGO, 10 mM N-TrGO, 50 mM N-TrGO, and NH_3 N-TrGO; (b) schematic of the electronic structure of TrGO, N-doped TRGO, and B-doped TrGO.

tendency. However, the gate-dependent S of B-TrGO and N-TrGO differed slightly from that of TrGO. In the case of 10 (50) mM B-TrGO, the gate-dependent S changed from 0 (−4) to 12 (20) μV K^{-1}, respectively, in a similar gate-bias range. Even though V_{Gate} was applied with a positive bias, which is electron-transport inducing, most charge carriers were holes, except in the case of 50 mM B-TrGO at $V_{Gate} > 40$ V. As previously noted, B was doped into TrGO and hole transport of B-TrGO appeared to be more intensive than that of TrGO. Conversely, the S of N-TrGO doped with urea changed from −10 to 4 μV K^{-1} in a similar gate-bias range. No significant change of the S was observed between the 10 mM and the 50 mM N-TrGO. However, for heavily doped N-TrGO (NH_3 N-TrGO), the S changed from −18 to −8 μV K^{-1} in a similar gate-bias range. Because of the N doping on TrGO, most of the charge carriers were electrons. The S values of TrGO, 10 mM B-TrGO, 50 mM B-TrGO, 10 mM N-TrGO, 50 mM N-TrGO, and NH_3 N-TrGO at 303 K and with $V_{Gate} = 0$ V were 1.09, 4.93, 7.22, −7.12, −4.7, and −13.29 μV K^{-1}, respectively. The S values of TrGO, 10 mM B-TrGO, and 50 mM B-TrGO at $V_{Gate} = 0$ V were positive, and the absolute value of the S increased after B doping. In addition, the charge-neutrality points of the TrGO, 10 mM B-TrGO, and the 50 mM B-TrGO were located at approximately 20, 50, and 80 V with gate bias, respectively. By contrast, the S values of the 10 mM N-TrGO, 50 mM N-TrGO, and NH_3 N-TrGO at $V_{Gate} = 0$ V were negative, and the charge-neutrality points of the 10 mM N-TrGO and 50 mM N-TrGO were at −40 V with gate bias. The charge-neutrality point of NH_3 N-TrGO was difficult to determine. The S of TrGO is consistent with Mott's equation, which predicts that conduction is determined by the Fermi level of a material. From the S at $V_{Gate} = 0$ V and the position of the charge-neutrality point, an electronic structure can be visualized in which the Fermi levels of TrGO and B-doped TrGO are located above the conduction-band edge, whereas the Fermi level of N-doped TrGO is located below the valence-band edge. Even though multi-layered graphene has a complicated electronic structure, it S is determined by the shape of density of states and the position of the Fermi level. As such, the Fermi levels of TrGO, 10 mM B-TrGO, 50 mM B-TrGO, 10 mM N-TrGO, 50 mM N-TrGO, and NH_3 N-TrGO can be distinguished and classified by exploring the gate-dependent S, as illustrated in Fig. 6(b).

Conclusions

Thermally activated carrier transport in TrGO, B-doped TrGO, and N-doped TrGO was investigated as a function of energy level. The doping degree was controlled by the amount of boric acid or urea added to the GO solution, and NH_3 gas was used to prepare heavily N-doped TrGO. The transfer curves indicated that hole transport in TrGO and B-doped TrGO was more intensive than electron transport, whereas electron transport was enhanced in N-doped TrGO. The relative bandgaps were obtained from the Arrhenius plots, and bandgap opening was found with both B- and N-doped TrGO. The gate-dependent S of TrGO showed both electron and hole transport, which shows ambipolar behavior. However, the gate-dependent S coefficients of B- and N-doped TrGO were slightly different. In the case of the gate-dependent S of B-doped TrGO, the S indicated that hole transport was predominant, even though an electron-transport-inducing gate bias was applied. However, in the case of the gate-dependent S of N-doped TrGO, the S indicated that electron transport was predominant, even though a hole-transport-inducing gate bias was applied. Interestingly, the S of heavily N-doped TrGO indicated intensive electron transport at both electron- and hole-inducing gate biases. Furthermore, the gate-dependent S showed a shift of the Fermi level as a function of the doping degree. Because the TrGO and B- or N-doped TrGO were found to exhibit metallic conduction, their S values are consistent with Mott's equation. By surveying the gate-dependent S values of TrGO and B- or N-doped TrGO, we inferred the relative position of their Fermi levels. The approach developed in this investigation allows the thermoelectric performance of materials to be speculatively predicted by understanding their electronic structure.

Conflicts of interest

There are no conflicts to declare.

Acknowledgements

This research was supported by the Basic Science Research Program through the National Research Foundation of Korea (NRF) funded by the Ministry of Science and ICT (NRF-2017R1A2B2010552 and 2015R1A5A7037615). We thank Prof. Mijung Lee for the use of the probe station.

References

1 C. R. Ocier, K. Whitham, T. Hanrath and R. D. Robinson, *J. Phys. Chem. C*, 2014, **118**, 3377–3385.

Published on 15 June 2018. Downloaded by Korea Institute of Science and Technology / KIST on 10/31/2019 6:27:51 AM.

2 S. J. Oh, Z. Wang, N. E. Berry, J.-H. Choi, T. Zhao, E. A. Gaulding, T. Paik, Y. Lai, C. B. Murray and C. R. Kagan, *Nano Lett.*, 2014, **14**, 6210–6216.
3 M. S. Kang, A. Sahu, D. J. Norris and C. D. Frisbie, *Nano Lett.*, 2011, **11**, 3887–3892.
4 R. H. Friend, R. W. Gymer, A. B. Holmes, J. H. Burroughes, R. N. Marks, C. Taliani, D. D. C. Bradley, D. A. D. Santos, J. L. Bredas, M. Logdlund and W. R. Salaneck, *Nature*, 1999, **397**, 121–128.
5 H. Sirringhaus, T. Kawase, R. H. Friend, T. Shimoda, M. Inbasekaran, W. Wu and E. P. Woo, *Science*, 2000, **290**, 2123–2126.
6 K. K. Banger, Y. Yamashita, K. Mori, R. L. Peterson, T. Leedham, J. Rickard and H. Sirringhaus, *Nat. Mater.*, 2010, **10**, 45.
7 M. D. Schroer and J. R. Petta, *Nano Lett.*, 2010, **10**, 1618–1622.
8 N. Shin, J. Kang, L. J. Richter, V. M. Prabhu, R. J. Kline, D. A. Fischer, D. M. DeLongchamp, M. F. Toney, S. K. Satija, D. J. Gundlach, B. Purushothaman, J. E. Anthony and D. Y. Yoon, *Adv. Funct. Mater.*, 2013, **23**, 366–376.
9 H. Fritzsche, *Solid State Commun.*, 1971, **9**, 1813–1815.
10 Y. M. Zuev, W. Chang and P. Kim, *Phys. Rev. Lett.*, 2009, **102**, 096807.
11 F. Ghahari, H.-Y. Xie, T. Taniguchi, K. Watanabe, M. S. Foster and P. Kim, *Phys. Rev. Lett.*, 2016, **116**, 136802.
12 D. Wang and J. Shi, *Phys. Rev. B*, 2011, **83**, 113403.
13 S. Das Sarma, S. Adam, E. H. Hwang and E. Rossi, *Rev. Mod. Phys.*, 2011, **83**, 407–470.
14 J. Hu, T. Wu, J. Tian, N. N. Klimov, D. B. Newell and Y. P. Chen, *Nano Energy*, 2017, **40**, 42–48.
15 M. Park, S. J. Hong, K. H. Kim, H. Kang, M. Lee, D. H. Jeong, Y. W. Park and B. H. Kim, *Appl. Phys. Lett.*, 2017, **111**, 173103.
16 S. Cho, S. D. Kang, W. Kim, E.-S. Lee, S.-J. Woo, K.-J. Kong, I. Kim, H.-D. Kim, T. Zhang, J. A. Stroscio, Y.-H. Kim and H.-K. Lyeo, *Nat. Mater.*, 2013, **12**, 913–918.
17 J. Park, G. He, R. M. Feenstra and A.-P. Li, *Nano Lett.*, 2013, **13**, 3269–3273.
18 N. Xiao, X. Dong, L. Song, D. Liu, Y. Tay, S. Wu, L.-J. Li, Y. Zhao, T. Yu, H. Zhang, W. Huang, H. H. Hng, P. M. Ajayan and Q. Yan, *ACS Nano*, 2011, **5**, 2749–2755.
19 J. Y. Park, U. Male and D. S. Huh, *Macromol. Res.*, 2017, **25**, 849–855.
20 K.-Y. Shin, S. Y. Lee and S.-S. Lee, *Macromol. Res.*, 2016, **24**, 170–175.
21 A. Ganguly, S. Sharma, P. Papakonstantinou and J. Hamilton, *J. Phys. Chem. C*, 2011, **115**, 17009–17019.
22 N. Kang and S. I. Khondaker, *Appl. Phys. Lett.*, 2014, **105**, 223301.
23 P. V. Kumar, M. Bernardi and J. C. Grossman, *ACS Nano*, 2013, **7**, 1638–1645.
24 J. Choi, N. K. Tu, S.-S. Lee, H. Lee, J. Kim and H. Kim, *Macromol. Res.*, 2014, **22**, 1104–1108.
25 N. D. K. Tu, J. Choi, C. R. Park and H. Kim, *Chem. Mater.*, 2015, **27**, 7362–7369.
26 K. P. Pernstich, B. Rössner and B. Batlogg, *Nat. Mater.*, 2008, **7**, 321.
27 D. Venkateshvaran, A. J. Kronemeijer, J. Moriarty, D. Emin and H. Sirringhaus, *APL Mater.*, 2014, **2**, 032102.
28 D. Venkateshvaran, M. Nikolka, A. Sadhanala, V. Lemaur, M. Zelazny, M. Kepa, M. Hurhangee, A. J. Kronemeijer, V. Pecunia, I. Nasrallah, I. Romanov, K. Broch, I. McCulloch, D. Emin, Y. Olivier, J. Cornil, D. Beljonne and H. Sirringhaus, *Nature*, 2014, **515**, 384–388.
29 J. P. Small, K. M. Perez and P. Kim, *Phys. Rev. Lett.*, 2003, **91**, 256801.
30 K. Yanagi, S. Kanda, Y. Oshima, Y. Kitamura, H. Kawai, T. Yamamoto, T. Takenobu, Y. Nakai and Y. Maniwa, *Nano Lett.*, 2014, **14**, 6437–6442.
31 C.-H. Lee, G.-C. Yi, Y. M. Zuev and P. Kim, *Appl. Phys. Lett.*, 2009, **94**, 022106.
32 S. Roddaro, D. Ercolani, M. A. Safeen, S. Suomalainen, F. Rossella, F. Giazotto, L. Sorba and F. Beltram, *Nano Lett.*, 2013, **13**, 3638–3642.
33 S. J. Choi, B.-K. Kim, T.-H. Lee, Y. H. Kim, Z. Li, E. Pop, J.-J. Kim, J. H. Song and M.-H. Bae, *Nano Lett.*, 2016, **16**, 3969–3975.
34 J. Wu, H. Schmidt, K. K. Amara, X. Xu, G. Eda and B. Özyilmaz, *Nano Lett.*, 2014, **14**, 2730–2734.
35 W. S. Hummers and R. E. Offeman, *J. Am. Chem. Soc.*, 1958, **80**, 1339.
36 D.-Y. Yeom, W. Jeon, N. D. K. Tu, S. Y. Yeo, S.-S. Lee, B. J. Sung, H. Chang, J. A. Lim and H. Kim, *Sci. Rep.*, 2015, **5**, 9817.
37 M. Xing, W. Fang, X. Yang, B. Tian and J. Zhang, *Chem. Commun.*, 2014, **50**, 6637–6640.
38 T. Wu, H. Shen, L. Sun, B. Cheng, B. Liu and J. Shen, *New J. Chem.*, 2012, **36**, 1385–1391.
39 Y.-B. Tang, L.-C. Yin, Y. Yang, X.-H. Bo, Y.-L. Cao, H.-E. Wang, W.-J. Zhang, I. Bello, S.-T. Lee, H.-M. Cheng and C.-S. Lee, *ACS Nano*, 2012, **6**, 1970–1978.
40 D. J. Late, A. Ghosh, K. S. Subrahmanyam, L. S. Panchakarla, S. B. Krupanidhi and C. N. R. Rao, *Solid State Commun.*, 2010, **150**, 734–738.
41 T. Schiros, D. Nordlund, L. Pálová, D. Prezzi, L. Zhao, K. S. Kim, U. Wurstbauer, C. Gutiérrez, D. Delongchamp, C. Jaye, D. Fischer, H. Ogasawara, L. G. M. Pettersson, D. R. Reichman, P. Kim, M. S. Hybertsen and A. N. Pasupathy, *Nano Lett.*, 2012, **12**, 4025–4031.
42 H. Bark, M. Ko, M. Lee, W. Lee, B. Hong and H. Lee, *ACS Sustainable Chem. Eng.*, 2018, **6**, 7468–7474.
43 J. H. Chen, C. Jang, S. Adam, M. S. Fuhrer, E. D. Williams and M. Ishigami, *Nat. Phys.*, 2008, **4**, 377–381.
44 A. L. Jain, *Phys. Rev.*, 1959, **114**, 1518–1528.
45 T. Ohta, A. Bostwick, J. L. McChesney, T. Seyller, K. Horn and E. Rotenberg, *Phys. Rev. Lett.*, 2007, **98**, 206802.
46 K. S. Kim, A. L. Walter, L. Moreschini, T. Seyller, K. Horn, E. Rotenberg and A. Bostwick, *Nat. Mater.*, 2013, **12**, 887.
47 J. Moon, J.-H. Kim, Z. C. Y. Chen, J. Xiang and R. Chen, *Nano Lett.*, 2013, **13**, 1196–1202.
48 Y. Saito, T. Iizuka, T. Koretsune, R. Arita, S. Shimizu and Y. Iwasa, *Nano Lett.*, 2016, **16**, 4819–4824.
49 M. Yoshida, T. Iizuka, Y. Saito, M. Onga, R. Suzuki, Y. Zhang, Y. Iwasa and S. Shimizu, *Nano Lett.*, 2016, **16**, 2061–2065.
50 S. Shimizu, T. Iizuka, K. Kanahashi, J. Pu, K. Yanagi, T. Takenobu and Y. Iwasa, *Small*, 2016, **12**, 3388–3392.

 This journal is © The Royal Society of Chemistry 2018